International Journal of Energy and Environmental Engineering
a SpringerOpen Journal

ORIGINAL RESEARCH Open Access

Load evaluation of horizontal-axis wind turbine rotor using coupled Beddoes near-wake model and free-wake method

Abdelfattah Bouatem[1*], Ahmed Almers[2] and Noureddine Boutammachte[2]

Abstract

Wind turbines operate mostly in yaw conditions that give rise to cyclic variations in aerodynamic forces applied on the blade. This induced load fluctuation is closely related to the upstream velocity field of the rotor and can be a significant source of fatigue and vibration. An accurate prediction of blade loading is considered the key in designing reliable and efficient wind turbines. The related calculation remains a complicated task to perform and requires enormous computing time. In this context, a numerical method is presented, aimed at evaluating the azimuthal fluctuation of the normal force. This method is obtained by coupling the Beddoes near-wake model and the free-wake method: the near-wake-induced velocities are calculated using Beddoes near-wake model with the far-wake contribution evaluated using the free-wake method. In addition, the unsteady effects on the aerodynamic coefficients are taken into account using the Beddoes-Leishman dynamic stall model. A computer code was developed, and numerical values were obtained in acceptable computational time. Results are compared with measurements performed in the NASA Ames wind tunnel.

Keywords: Wind turbine; Yaw; Skewed wake; Stall delay; Free wake; Near wake; Far wake

Background

To reach satisfactory levels of performance, the horizontal-axis wind turbine requires accurate predictions of the aerodynamic forces acting on the blades. However, in non-steady conditions, these aerodynamic load predictions remain a complicated task to perform because of the complex nature of the flow around the blades.

To model the wind turbine, a variety of mathematical models exist, such as the blade element method (BEM), computational fluid dynamics (CFD) method, and vortex method, each with different levels of accuracy and complexity.

The classical BEM method is obtained by coupling blade element theory with momentum theory [1]. This method assumes that the blade can be divided into several elements. The study is performed for each element by applying the momentum theory in the axial and tangential direction. The BEM method includes several approximations and limitations. Its validity may be extended using empirical corrections to take into account the finite number of blades, blade tip losses, and the cyclical variation of the axial induction factor in yaw conditions.

Currently, the use of the CFD techniques has experienced significant progress thanks to the improved performance of computers. Despite the accurate results obtained in most cases, CFD methods require huge computational resources and large memory.

The aim of the vortex theory is to model the wind turbine taking into account the geometry of the wake behind the rotor and its effect on the velocity field upstream [2]. The vortex theory principle is derived from the lifting line and lifting surface theories, which have been developed for airplane wings to determine wing loads and wake geometry. The flow is replaced by inviscid and incompressible fluid through an equivalent vortex system. The methodology is based on the Biot-Savart law to compute induced velocities and the vorticity transport theorem to shape the wake which is generally divided into near wake and far wake. The near wake consists of the trailing vortices issuing from the trailing

* Correspondence: Bouatem1@hotmail.com
[1]Department of Mechanical Engineering, Moulay Ismail University, ENSAM-MEKENS, PO. BOX. 4024, Meknes 50003, Morocco
Full list of author information is available at the end of the article

edges. The far wake is reduced in two intense tip and root vortices.

The vortex method gives more accurate results than the BEM method and is relatively easy to implement compared with CFD methods. Consequently, the vortex theory can be a better choice for predicting the aerodynamic performance of a wind turbine. This methodology requires a perfect determination of the wake geometry. There are two main approaches to shape the wake. The first is known as 'prescribed wake.' According to this method, the wake geometry is known *a priori*. The second is the 'free-wake method,' which is based on the following steps: first, trailing vortices are detached from the blade and represented by Lagrangian markers; then, the wake-induced velocities are calculated using the Biot-Savart law at each Lagrangian marker to determine their new positions; finally, the Lagrangian markers are connected by a straight line to form the wake [3]. This method requires huge computational time, basically at the near-wake region. This can be explained by the large number of trailing vortices and straight lines which form the wake.

The main objective of this paper is to develop a numerical procedure that can predict aerodynamic loads without using great amounts of computer time which are generally required in the free-wake method. This procedure is obtained by combining the Beddoes near-wake model with the free-wake method. The Beddoes near-wake model is used to calculate the near-wake-induced velocities at the rotor plane. The free-wake method is used to shape the far wake in a simpler and faster way; the calculation begins with a generation of a rigid wake which is corrected to take into account the effect of wake-induced velocities.

The near-wake-induced velocities are added to the far-wake-induced velocities to calculate the circulation distribution along the blade. This iterative procedure continues until the rotor flow field takes a constant value. The wind turbine is assumed to be operating in yaw conditions. To take into account the unsteady aerodynamic effect on the blade loading, the Beddoes-Leishman dynamic stall model has been used. In this model, the deficiency in lift arising from the circulatory effect of shed vorticity is modeled using the indicial response function. To validate this numerical simulation, a comparison is made with measurements performed in the NASA Ames wind tunnel.

Methods

Beddoes near-wake model

The Beddoes near-wake model is designed to approximate the single blade near-wake contribution to the downwash using exponential functions. This model covers the first quadrant of the vortex life. After this first quarter of a revolution, the trailing vortices are supposed to be in the process of rolling-up [4]. The shed vorticity is not included in the Beddoes near-wake model but introduced in the calculation using the Beddoes-Leishman dynamic stall model.

As shown in Figure 1, the vortex element of length ds, strength Γ, and originating from the point B, induces the velocity dw at point A. Assuming that the geometry of the near-wake vortices can be approximated by a circular arc, the induced velocity dw can be expressed according to:

$$dw = \frac{\Gamma \cdot ds}{4 \cdot \pi \cdot r^2} \quad \frac{1 - \left(1 - \frac{h}{r}\right) \cdot \cos(\Omega)}{\left[1 + \left(1 - \frac{h}{r}\right)^2 - 2 \cdot \left(1 - \frac{h}{r}\right) \cdot \cos(\Omega)\right]^{3/2}} \quad (1)$$

Beddoes suggested approximating the equation with a series of exponential functions [4]. The axial contribution at the *i*th time step to the downwash from one circular arc is given by

$$w(i) = \sum_{k=1}^{n} Z_K(i) \quad (2)$$

$$Z_K(i) = Z_k(i-1) \cdot e^{b_k \frac{\Delta\Omega}{\varphi}} + c_k \cdot D_w \cdot e^{b_k \frac{\Delta\Omega}{2 \cdot \varphi}}$$

$$\varphi = \frac{\pi}{4} \left| \left(1 + \frac{h}{2 \cdot r}\right) \ln\left(1 - \frac{h}{r}\right) \right|$$

$$D_w = \frac{\Gamma \left| \Delta\Omega \frac{r}{h} \right| \cos(\chi)}{4 \pi h \sqrt{1 + \left(\Delta\Omega \frac{r}{h}\right)^2}}$$

The Beddoes near-wake model is based on the assumption that the near-wake-trailed vortices remain in the rotor plane. Wang and Coton have developed an extension of the previous model to take into account a tilting angle χ [5]:

$$\tan(\chi) = \frac{V_\infty \cos\left(\Phi_y\right) + w_B}{\omega \cdot r + V_\infty \cdot \sin\left(\Phi_y\right) \cdot \sin\left(\Phi_r\right) + u_B} \quad (3)$$

where w_B and u_B are, respectively, the axial and tangential velocities at point B, ω the angular velocity, and V_∞ the free-stream velocity.

The near-wake tangential induced velocity (w) is calculated in the same way as the axial induced velocity:

$$w'(i) = \sum_{k=1}^{n} Z'_k(i) \quad (4)$$

$$Z'_K(i) = Z'_K(i-1) \cdot e^{b_k \frac{\Delta\Omega}{\varphi}} + c_k \cdot D_w \cdot e^{b_k \frac{\Delta\Omega}{2 \cdot \varphi}}$$

$$D'_w = \frac{\Gamma \left| \Delta\Omega \frac{r}{h} \right| \sin(\chi)}{4 \pi h \sqrt{1 + \left(\Delta\Omega \frac{r}{h}\right)^2}}$$

Each vortex is divided into several elements, and the total contribution of the vortex is calculated using the trapeze method at each time step. The circulation is

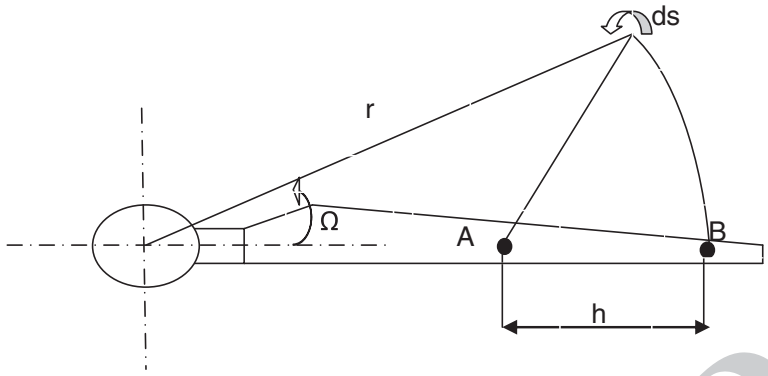

Figure 1 Beddoes near-wake geometry.

calculated at each blade element using the Kutta-Joukowski law [6]:

$$\Gamma = \frac{1}{2} V_{\mathrm{rel}} \cdot C \cdot C_{\mathrm{l}}(\alpha)$$

where $C_{\mathrm{l}}(\alpha)$ is the lift coefficient, V_{rel} the relative velocity, C the cord, and Γ the circulation.

Far-wake modeling

This part of the wake consists of two vortices issuing from the blade tip and root. The trailing vortices shed from the leading edge sections are assumed to join together to form a strong tip and root vortex.

This rolling-up process takes place after the first-quarter revolution from their generation.

To model the far wake, the problem is investigated in two coordinate systems, as depicted in Figure 2, a blade-fixed Cartesian coordinate system (x,y,z) and a plane-fixed coordinate system (X,Y,Z) on the rotor disk.

Two different types of wake geometry are successively used during the calculation: a rigid wake and a free wake. The rigid wake is used to initialize the calculation and to give an initial geometry to the free wake. The free wake is based on the Prandtl lifting line theory. The vortices are represented by Lagrangian markers which are connected by straight line vortex segments, as represented in Figure 3.

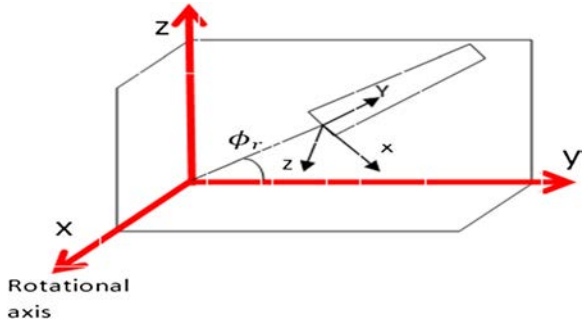

Figure 2 Coordinate systems for wind turbine rotor.

The positions of the markers are obtained by solving the transport equation using a second-order predictor/corrector scheme.

The rigid wake model assumes that the wake is convected by free-stream velocity. As a result, the flow behind the rotor consists of helical wake with constant pitch and diameter. The rigid wake is obtained from:

$$\vec{r}: \begin{cases} X_{\mathrm{V}} = V_{\infty} \dfrac{\Psi_{\mathrm{b}}}{\Omega} \\ Y_{\mathrm{V}} = R \cdot \cos(\Psi_{\mathrm{w}}) \\ Z_{\mathrm{V}} = R \cdot \sin(\Psi_{\mathrm{w}}) \end{cases} \tag{5}$$

where R is the blade radius and $\vec{r}$ is the position vector of collocation point (p) that can be represented using two variables Ψ_{b} and Ψ_{w} (being a measure of azimuth and a measure of wake age, respectively).

The initial helical geometry has to be distorted under the influence of induced velocities. The fundamental equation describing the transport of Lagrangian markers is

$$\frac{d\vec{r}}{dt} = \vec{W} \tag{6}$$

where $\vec{W}$ is the geometrical sum of local induced velocities generated by the different parts of the wake and the wind free-stream velocity.

For the rotating blade application, the governing Equation 6 can be written in the form of first-order partial differential equation:

$$\frac{\partial r}{\partial \psi_w} + \frac{\partial r}{\partial \psi_{\mathrm{b}}} = \frac{1}{\Omega} \cdot W \tag{7}$$

The induced velocity terms are highly nonlinear [7]. Therefore, the velocity transport Equation 7 cannot be solved analytically; numerical tools must be adopted. The solution is accomplished by discretizing the problem and transforming the governing Equation 7 into a finite

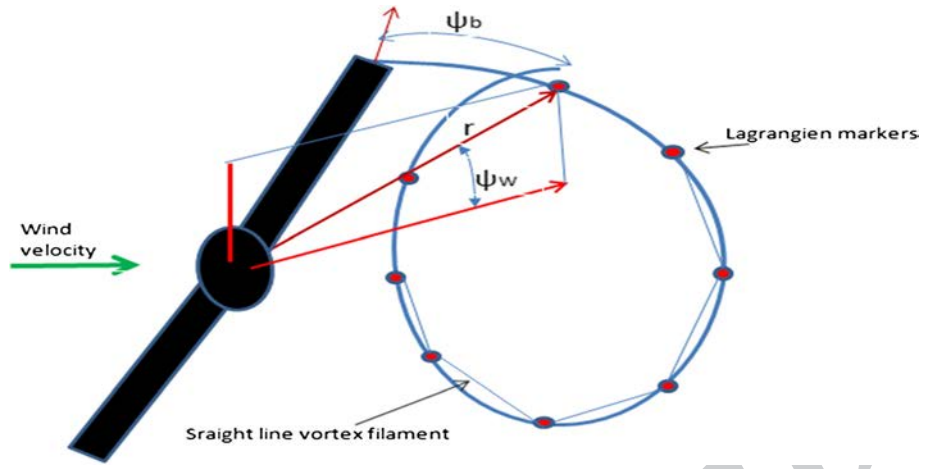

Figure 3 Representation of rotor wake.

difference equation. In the present work, a five-point central differencing scheme has been adopted. The discretized equation can be written as:

$$\overrightarrow{r_{i,j}} = \overrightarrow{r_{i-1,j-1}} + \left(\overrightarrow{r_{i,j-1}} - \overrightarrow{r_{i-1,J}}\right)\left(\frac{\Delta\Psi_w - \Delta\Psi_b}{\Delta\Psi_w + \Delta\Psi_b}\right) + \frac{2}{\Omega}\left(\frac{\Delta\Psi_w \times \Delta\Psi_b}{\Delta\Psi_w + \Delta\Psi_b}\right)\vec{W} \quad (8)$$

The Biot-Savart law is used here to calculate the induced velocities at Lagrangian markers to determine their new positions [8]. As illustrated in Figure 4, the induced velocity field generated by an infinitesimal element (dl) of the vortex line (MN) at any point is calculated using:

$$\overrightarrow{dV_{\text{induced}}} = \frac{\Gamma}{4\pi}\frac{\vec{dl} \wedge \vec{h}}{|h|^3} \quad (9)$$

The Biot-Savart law must be integrated to calculate the induced velocity generated by vortex line (MN). Referring to the Figure 4, Equation 9 can be written as

$$\overrightarrow{dV_{\text{induced}}} = \frac{\Gamma}{4\pi}\frac{\vec{r_1} \wedge \vec{r_2}}{\left|\vec{r_1} \wedge \vec{r_2}\right|^2}\left[\frac{\vec{r_0} \cdot \vec{r_1}}{\left|\vec{r_1}\right|} - \frac{\vec{r_0} \cdot \vec{r_2}}{\left|\vec{r_2}\right|}\right] \quad (10)$$

Note that at any iteration, the circulation Γ is assumed to be constant along the vortex. This parameter is equal to the maximum value along the blade. Furthermore, the representation of the tip and root vortex by straight segments reduces the accuracy of the calculation. Indeed, the Biot-Savart equation shows singular behaviors when point P is located very near or coincides with the vortex filament (Figure 4). These singularities can be removed by multiplying the Biot-Savart law with a viscous parameter K_V [9].

$$K_V = \frac{H^2}{\left(r_c{}^2 + H^4\right)^{1/2}} \quad (11)$$

Bhagwat and Leishman [10] suggested an empirical approach to calculate the growth of the viscous core radius:

$$r_c = \sqrt{\frac{4 \cdot \alpha \cdot \nu \cdot \delta \cdot \Psi_w}{\Omega}}$$

The eddy-viscosity coefficients δ is expressed as a function of the Reynolds number as:

$$\delta = 1 + a_1 \cdot R_e$$

where α is Lamb-Oseen constant and a_1 is an empirical parameter.

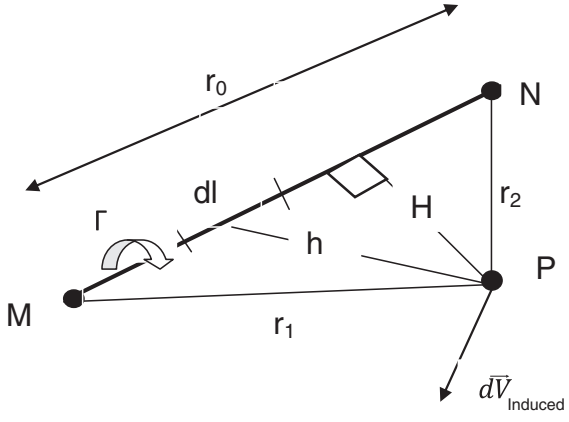

Figure 4 Velocity induced by a finite straight vortex.

Aerodynamic coefficients

The AERODAS model [11] is used to calculate the airfoil lift and drag coefficients, in both pre-stall and post-stall regimes, as functions of the angle of attack. The lift coefficient in the pre-stall regime is given by:

$$\text{if} \quad \alpha \geq A \qquad CL_1 = S1\cdot(\alpha - A0) - RCL\ 1\left(\frac{\alpha - A0}{ACL_1 - A0}\right)^{N_1}$$

$$\text{if} \quad \alpha < A_0 \quad CL_1 = S1\cdot(\alpha - A0) + RCL\ 1\left(\frac{-\alpha + A0}{ACL_1 - A0}\right)^{N_1}$$

where

$$RCL\ \ 1 = S1\cdot(ACL_1 - A0) - CL_{1\max}$$

$$N_1 = 1 + \frac{CL_{1\max}}{RCL1}$$

The drag coefficient in the pre-stall regime is obtained by following expressions:

$$\text{if} \quad (2\cdot A_0 - ACD_1) \leq \alpha \leq ACD_1$$

$$CD_1 = CD_0 + (CD_{1\max} - CD_0)\cdot\left(\frac{\alpha - A0}{ACD_1 - A0}\right)^{M}$$

$$\text{if} \quad \alpha < (2\cdot A_0 - ACD_1) \ \text{ or } \ \alpha > ACD_1 \qquad CD_1 = 0$$

The lift coefficient in the post-stall regime is expressed as follows:

$$\text{if} \quad 0 < \ \alpha < ACL_1 \qquad CL_2 = 0$$

$$\text{if} \quad ACL_1 \leq \alpha \leq 92.0^{\circ} \qquad CL_2 = -0.032\cdot(\alpha - 92) - RCL\ 2\cdot\left(\frac{92 - \alpha}{51}\right)^{N_2}$$

$$\text{if} \quad \alpha > 92.0^{\circ} \qquad CL_2 = -0.032\cdot(\alpha - 92) + RCL\ 2\cdot\left(\frac{-92 + \alpha}{51}\right)^{N_2}$$

where

$$RCL2 = 1.632 - CL_{2\max}$$

$$N_2 = 1 + \frac{CL_{2\max}}{RCL2}$$

The drag coefficient in the post-stall regime is given by the following equations:

$$\text{if} \quad (2\cdot A_0 - ACL_1) < \alpha < ACL_1 \qquad CD_2 = 0$$

$$\text{if} \quad \alpha \geq ACD_1 \qquad CD_2 = -CD_{1\max} + (CD_{2\max} - CD_{1\max})\ COS\ \left(\frac{90 - \alpha}{90 - ACD1}\cdot 90\right)$$

Figure 5 shows the calculated aerodynamic coefficient using AERODAS model.

Dynamic stall

Dynamic stall is one of the consequences of an unstable aerodynamic environment. When the angle of attack changes rapidly, the aerodynamic forces differ from their static values. Also, the cyclical variation of the angle of attack produces a significant hysteresis which affects the aerodynamic loads applied on the blade. Dynamic stall is of great importance in practice. In most cases, this is the first factor to consider in determining the performance of structures exposed to flows.

The Beddoes-Leishman models are semi-empirical equations based on airfoil indicial response. These indicial functions compute the non-steady aerodynamic coefficients as a function of angle of attack change in a sample time interval. This method is based on the superposition of three distinct parts [12]:

- Attached flow
- Separated flow
- Leading-edge separation.

Attached flow module In non-steady attached flow, the aerodynamic forces acting on an airfoil can be divided in two components, circulatory and impulsive. The circulatory component is linked to the existing vortices on the airfoil; it is given by [13]:

$$C^{c}_{N,n} = C_{N\alpha}\cdot\ \alpha_{eq,n} \tag{12}$$

$$\alpha_{eq,n} = \alpha_n\ -\ X_n\ - Y_n$$

$$X_n = X_{n-1}\cdot\exp(-b_1\Delta S) + A_1\cdot\Delta\alpha_n\exp(-b_1\Delta S/2)$$

$$Y_n = Y_{n-1}\cdot\exp(-b_2\Delta S) + A_2\cdot\Delta\alpha_n\exp(-b_2\Delta S/2)$$

$$\Delta S = \frac{2\cdot U\cdot\Delta t}{C}$$

where $\Delta\alpha_n$ is the change in the angle of attack over a sample interval Δt, C is the cord, U is the free-stream velocity, and A_1, A_2, b_1, and b_2 are empirical constants.

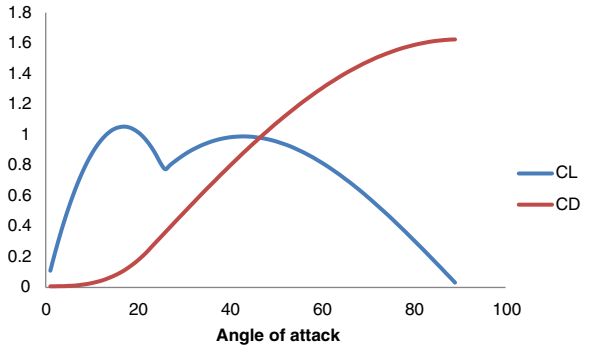

Figure 5 Calculated lift and drag coefficients for NREL S809.

The magnitude of the impulsive normal force coefficient can be obtained with:

$$C^{I}_{N,n} = \frac{3 \cdot C}{V_{eff}} \cdot \left(\frac{\Delta \alpha_n}{\Delta t} - D_n \right) \tag{13}$$

$$D_n = D_{n-1} \cdot \exp\left(-\frac{\Delta t}{K_\alpha T_1} \right) + \left(\frac{\Delta \alpha_n - \Delta \alpha_{n-1}}{\Delta t} \right) \exp\left(-\frac{\Delta t}{2 K_\alpha T_1} \right)$$

$$T_1 = \frac{C}{A}$$

$$K_\alpha = \frac{0.75}{(1-M)} + \pi \; g^2 M^2 (A_1 b_1 + A_2 b_2)$$

$$g = \left(1 - M^2\right)^{1/2}$$

where V_{eff} is the effective velocity, C represents the airfoil cord, A is the sound velocity, and M the Mach number.

The total normal force coefficient for attached flow is given by:

$$C^{P}_{N,n} = C^{I}_{N,n} + C^{C}_{N,n} \tag{14}$$

Trailing edge separation module Trailing edge separation is the gradual separation of the boundary layer from the surface of the aerofoil.

The relation between the flow separation point f and the normal force coefficient is given by the Kirchhoff relation [14]:

$$C_N = C_{N\alpha} \cdot \left(\frac{1 + \sqrt{f}}{2} \right)^2 \alpha \tag{15}$$

where $C_{N\alpha}$ is the normal force coefficient slope near 0°. By inverting the Kirchhoff relation and using the airfoil's static characteristics, we obtain the static separation point as a function of angle of attack $f(\alpha)$.

In non-steady conditions, a delay must be introduced in the calculation of the normal force coefficient using:

$$C'_{N,n} = C_{N,n} - D_{p,n}$$

where the deficiency function is evaluated as follows:

$$D_{p,n} = D_{p,n-1} \cdot \exp\left(-\frac{\Delta S}{T_p} \right) + \left(C^{P}_{N,n} - C^{P}_{N,n-1} \right) \cdot \exp\left(-\frac{\Delta S}{2 T_p} \right)$$

with

$$T_P = 9$$

It is now possible to evaluate the effective angle of attack which provides the same leading edge pressure in the steady case using the following expression:

$$\alpha_{f,n}(t) = \frac{C'_{N,n} - C_{N_0}}{C_{N_\alpha}}$$

where C_{N0} is the normal force coefficient obtained when the angle of attack is equal to 0°. Using the static separation point characteristic, presented previously, we compute the effective separation point:

$$f'_n = f\left(\alpha_{f,n}\right)$$

The unsteady effect is taken into account in the calculation of the dynamic separation point according to:

$$f''_n = f'_n - D_{f,n}$$

The deficiency function is evaluated as:

$$D_{f,n} = D_{f,n-1} \cdot \exp\left(-\frac{\Delta S}{T_f} \right) + \left(f'_n - f'_{n-1} \right) \exp\left(-\frac{\Delta S}{2 T_f} \right)$$

with

$$T_f = 5$$

Finally, using the Kirchhoff relation, we compute the contribution of the trailing edge separation in the calculation of the normal force coefficient as:

$$C^{f}_{N,n} = C_{N\alpha} \cdot \left(\frac{1 + \sqrt{f''_n}}{2} \right)^2 \alpha_{\text{eq},n}$$

Leading edge separation The leading edge separation takes place in the following condition [15]:

$$C'_{N,n} > C_{N,I}$$

where $C_{\text{N,I}}$ represents the critical value of the normal force, obtained with C_{N} corresponding to the static break in the pitching moment.

The contribution of the leading edge separation $C^V_{N,n}$ is calculated using:

$$C^V_{N,n} = \begin{cases} C^V_{N,n-1}\cdot\exp\left(\frac{-\Delta S}{T_v}\right) + \left(C_{V,n}-C_{V,n-1}\right)\cdot\exp\left(\frac{-\Delta S}{2T_v}\right) & \text{if} \quad \alpha_n\frac{dC_V}{dt}\geq 0 \quad and \quad 0<\tau_{Vn}<2T_{vl} \\ C^V_{N,n-1}\cdot\exp\left(\frac{-\Delta S}{T_v}\right) & \end{cases} \tag{16}$$

$$C_{V,n} = C^C_{N,n}\ \left(1-K_{N,n}\right)$$

$$K_{N,n} = \left(\frac{1+\sqrt{f''_n}}{2}\right)^2$$

The non-dimensional vortex time parameter $\tau_{v,n}$ is given by:

$$\tau_{v,n} = \begin{cases} \tau_{v,n-1} + \frac{dt}{c/2}\cdot V_{\text{eff}}\cdot 0,45 & if\ C'_{N,n} > C_{N,I} \\ 0 \quad if \quad C'_{N,n} < C_{N,I} \ and \ \Delta\alpha_n > 0 & \end{cases}$$

Finally, the aerodynamic coefficients are given as follows:

$$C_{N,n} = C^f_{N,n} + \ C^V_{N,n} \ + \ C^I_{N,n}$$

$$C_{C,n} = \eta\cdot C_{N\alpha}\cdot\ \sqrt{f''_n}\alpha^2_{\text{eq},n}$$

$$\eta \approx\ 0.95$$

$$C_L = C_{N,n}\cdot\ \cos(\alpha)\ + C_{C,n}\cdot\ \sin(\alpha)$$

$$C_D = C_{N,n}\cdot\ \sin(\alpha)\ - C_{C,n}\cdot\ \cos(\alpha)$$

where $C_{N,n}$ is the normal force coefficient, $C_{C,n}$ is the tangential force coefficient, C_L is the lift coefficient, and C_D is the drag coefficient.

To verify the dynamic stall model, Figures 6 and 7 show the comparison between numerical results and experimental data [16] for different values of reduced frequency $k = \omega c/2V$. The pitching motion is given by $\alpha = Am\sin(\omega pt) + \alpha m$. This comparison demonstrates the ability of the Beddoes-Leishman dynamic stall model to predict the non-steady aerodynamic coefficients.

Computational algorithm

The algorithm presented in Figure 8 describes the computational procedure. First, the calculation begins with the evaluation of the near-wake-induced velocities. Second, when the first-quarter revolution has passed, the vortices are assumed to be in the rolling-up process to form the far wake.

The far-wake geometry is initialized with a rigid wake; we assume at this stage that the wake behind a rotor consists of a helical wake with constant pitch and diameter, because the effects of induced velocities are neglected. Afterward, the induced velocities are calculated at different Lagrangian markers, and the wake is corrected by the implementation of a predictor/corrector scheme. Finally, this new geometry is used in the calculation of induced velocities at the rotor plane. This iterative process continues until obtaining a constant value of the induced flow and circulation of the rotor plane.

As illustrated in the algorithm, the circulation is used in the calculation of induced velocities. This parameter is evaluated in terms of the lift coefficient using the Kutta-Joukozsky law.

In the present work, the wake simulation is based on the assumption that the flow is inviscid. However, the calculation of the aerodynamic coefficients by the AERODAS model takes into account the viscous effect which permits the modeling of stall. Also, the aerodynamic coefficients are corrected by the implementation of Beddoes-Leishman dynamic stall model to take into consideration the non-steady effect.

Results and discussion

In this section, some illustrative examples are presented to demonstrate the capability of the proposed method to

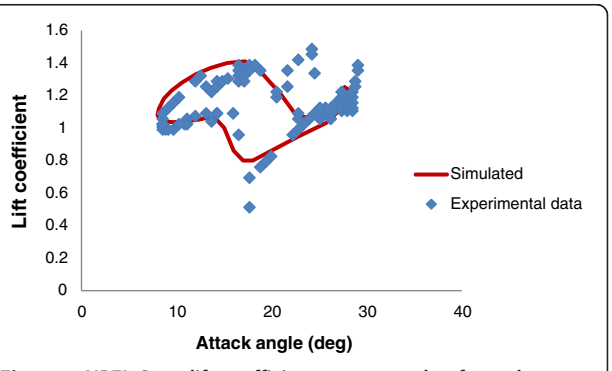

Figure 6 NREL S809 lift coefficient versus angle of attack; $\alpha = 20 + 10\sin(\omega t)$, $k = 0.025$, $M = 0.1$.

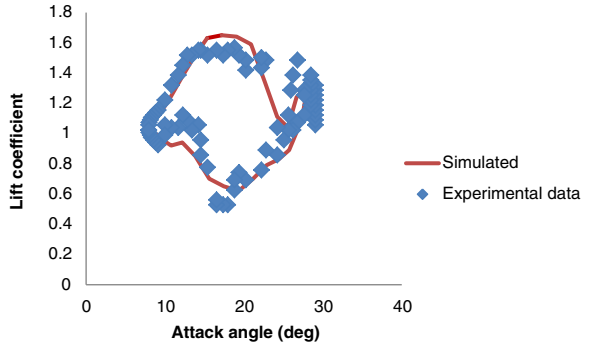

Figure 7 NREL S809 lift coefficient versus angle of attack; $\alpha = 20+10\sin(\omega t)$, $k = 0{,}051$, $M = 0.1$.

predict the variation of the normal force acting on the blade. Experimental results were obtained at the National Renewable Energy Laboratory in NASA Ames wind tunnel, where test conditions are rigorously controlled [17]. The NASA Ames wind tunnel possesses excellent test section flow quality. Flow speeds deviate by no more than 0.25% from the nominal value, whereas the flow velocity vector diverges no more than 0.5° from the test section axis. Turbulence intensity is typically no greater than 0.5%. The set speed value differed less than 0.1 m/s from the nominal value. The average pressure measurement system bias error was less than 0.22%.

Measurements were performed on a wind turbine operating in yaw conditions. This wind turbine was two bladed,

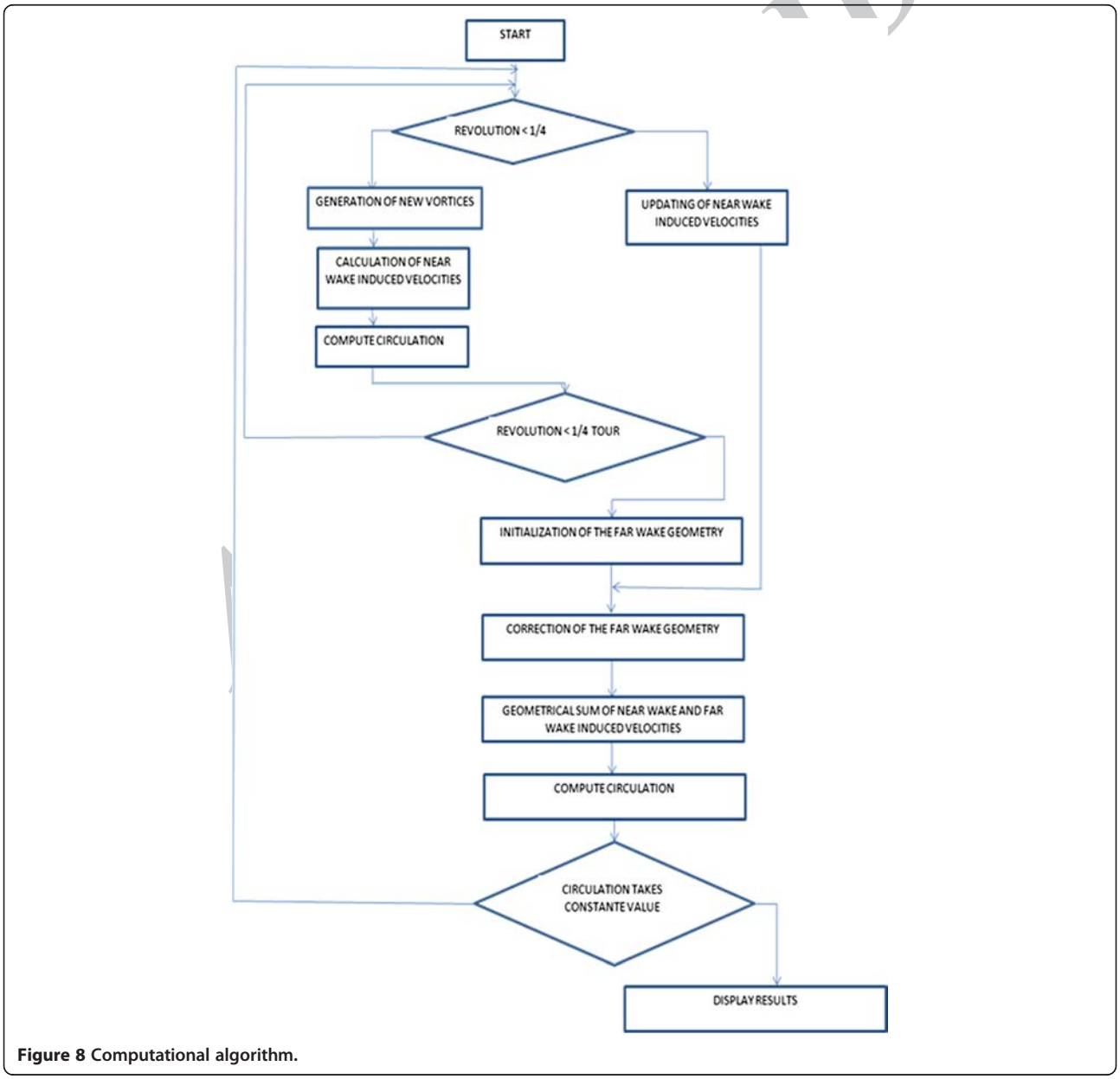

Figure 8 Computational algorithm.

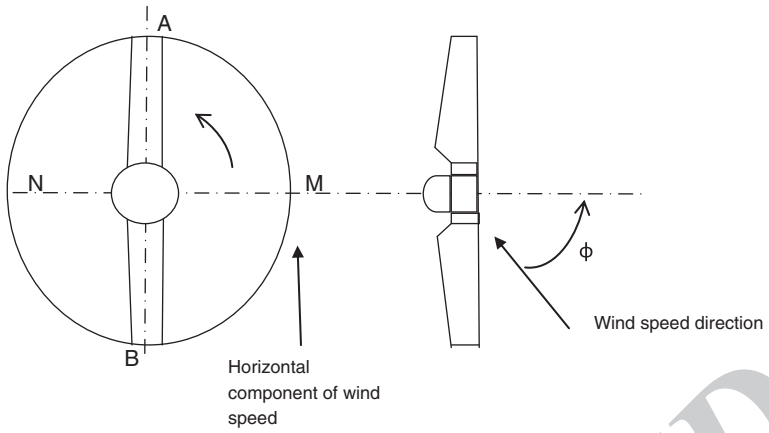

Figure 9 Advancing and retreating effect.

and it had a rotor diameter of 10 m. The yaw angle was equal to 30°, and the pitch angle was equal to 0°. The airfoil was of type S809 over the entire span [18].

Referring to Figure 9, the horizontal component of the wind velocity is not null in yaw conditions. This component must be taken into account in the calculation. Its projection in the blade-fixed Cartesian coordinate system can be expressed as $U \sin(\phi_y) \cos(\phi_r)$. Accordingly, the angle of attack is calculated with:

$$\alpha = a\tan\left(\frac{U\cos\left(\varphi_y\right) - U_{\text{induced}}}{\Omega\ r + W_{\text{induced}} + U\sin\left(\varphi_y\right)\ \cos\ \left(\varphi_r\right)}\right) - \beta$$

The relative wind velocity is calculated by using the following equation:

$$V_{\text{rel}} = \sqrt{\left(U\cos\left(\varphi_y\right) - U_{\text{induced}}\right)^2 + \left(\Omega\, r + W_{\text{induced}} \cdot U\sin\left(\varphi_y\right)\cos(\varphi_r)\right)^2}$$

where U_{induced} is the axial induced velocity and W_{induced} the tangential induced velocity.

In yaw conditions, we distinguish two main operating modes: the advancing and the retreating modes. The blade will be advancing in the half-plane (ANB) and retreating in the half-plane (BMA), as depicted in Figure 9. These mean that the horizontal component of the wind relative velocity is in opposition with the rotation vector in the half-plane ANB and in line with the rotation vector in the half-plane BMA. Consequently, the blade load, the relative velocity, and the angle of attack vary depending on the azimuthal position.

In the following, we represent the azimuthal variation of the normal force at 30% and 95% span of the blade to validate the algorithm and to better observe the influence of the skewed wake and the advancing and retreating behaviors.

Figures 10 and 11 show the distribution of the normal force at 30% and 95% span for an air speed of 5 m/s.

We observe that the calculated and measured curves are in perfect agreement. These are in phase and show the same tendencies.

The results presented in Figures 12 and 13 show the distribution of the normal force at 30% and 95% span for an air speed equal to 15 m/s. The agreement between

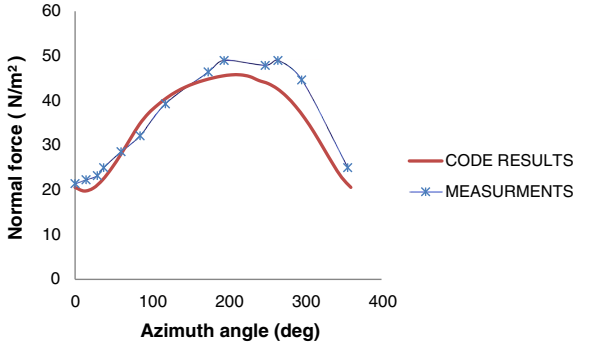

Figure 10 Normal force distribution at 30% span, for wind speed of 5 m/s.

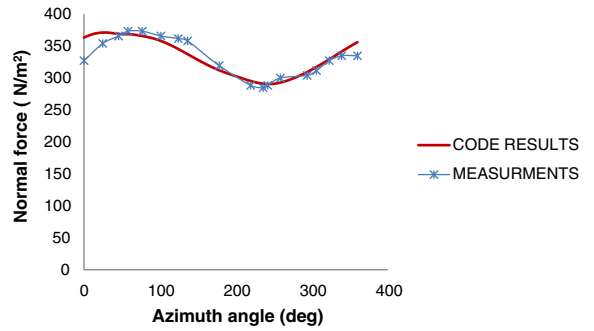

Figure 11 Normal force distribution at 95% span, for wind speed of 5 m/s.

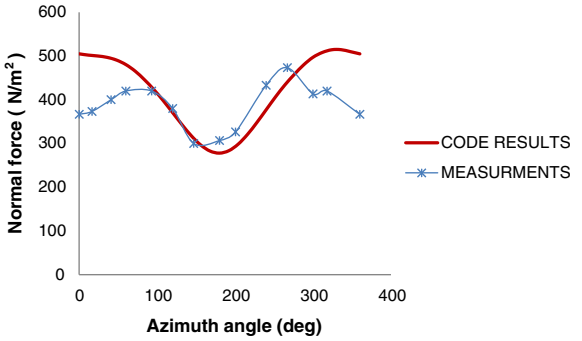

Figure 12 Normal force distribution at 30% span, for wind speed of 15 m/s.

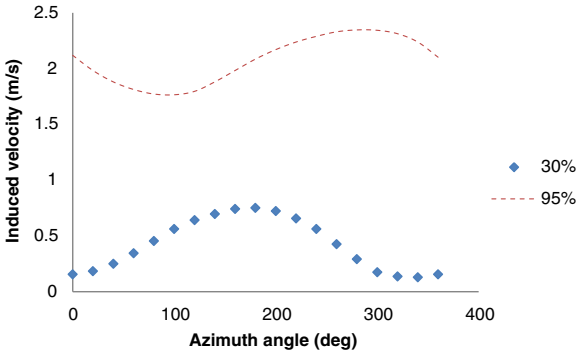

Figure 14 Azimuthal distribution of induced velocity for an air speed of 5 m.

measured and calculated curves is excellent in terms of shape despite the existence of an amplitude difference.

Prediction uncertainties, found at high wind speed, essentially originate from assumptions adopted in the modeling and the limits of models used to predict aerodynamic coefficient in the non-steady case. Furthermore, at high wind velocity, compressibility and turbulence become important. Consequently, the approach adopted in this work where the fluid is considered inviscid and incompressible can lead to significant discrepancies in results [17]. Also, the great number of empirical parameters used in the AERODAS model and the Beddoes-Leishman dynamic stall model could be a source of error. In this context, the study referenced in [19] confirmed that existing models show significant disparities at high wind velocity. This can be attributed to inconsistencies in empirical input parameters, which need to be derived from unsteady measurements for each and every airfoil, and over the appropriate ranges of the Reynolds and Mach numbers.

In contrast, the cyclical fluctuation of the normal force observed previously is mainly caused by the skewed wake effect and the advancing and retreating blade effect. To better illustrate the skewed wake effect, Figure 14 shows the variation of the induced velocities at 30% and 95% for an air speed of 5 m/s.

We note that there is a correlation between the distribution of the induced velocity presented in Figure 14 and the distribution of the normal force presented in Figures 10 and 11.

At the inboard section, the maximum value of the normal force is found between 180° and 360°. This behavior is consistent with the skewed wake effect because the minimum value of the induced velocity is found between 180° and 360°. For the outboard section, the maximum value of the normal force is found between 0° and 180°. This behavior is in line with the skewed wake effect presented in Figure 11 because the minimum of the induced velocity is found between 0° and 180°.

Generally speaking, for a wind speed of 5 m/s, the distribution of the normal force is mainly influenced by the skewed wake effect in spite of some disturbances caused by the contribution of the advancing and retreating blade effect.

Figure 15 shows the azimuthal variation of the relative velocity and horizontal component of the wind velocity for a wind speed of 15 m/s. We observe that the azimuthal variation of the horizontal component of the wind velocity

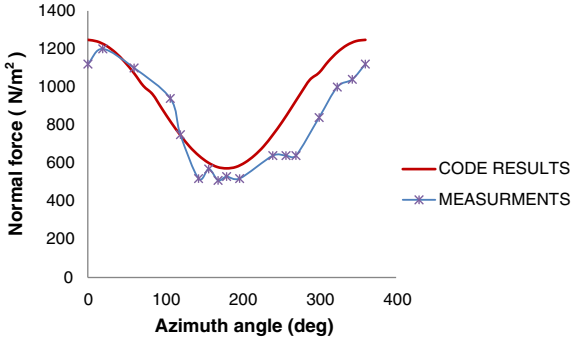

Figure 13 Normal force distribution at 95% span, for wind speed of 15 m/s.

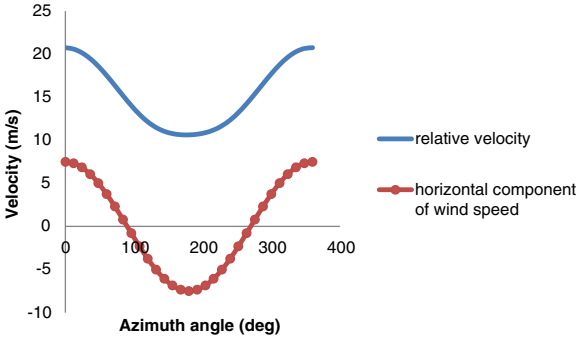

Figure 15 Azimuthal variation of relative velocity and horizontal component of wind velocity for wind speed of 15 m/s.

is reflected in the azimuthal variation of the normal force illustrated in Figures 12 and 13. We underline a correlation between these distributions.

We conclude that at high wind speeds, the variation of the normal force is mainly influenced by the advancing and retreating blade effect. This can be explained by the predominance of the advancing and retreating blade effect compared with the skewed wake effect.

Conclusion

We have developed a numerical code for a yaw-misaligned wind turbine. The numerical procedure is obtained by combining the Beddoes near-wake model and the free-wake method. The Beddoes-Leishman dynamic stall model was implemented in the calculation, and results of the complete model were compared with the NASA Ames wind tunnel measurements. This comparison demonstrates the capability of the models used to reproduce a physically realistic feature with acceptable tolerance. However, we have observed the existence of a difference in amplitude at high wind speed arising from the different assumptions adopted in this work.

The load fluctuation highlighted in this work is caused by the skewed wake effect and the advancing and retreating effect. The former plays a major role in the aerodynamic loads calculation at low wind speed. However, the latter is important at high wind speed and can provide a strong dynamic stall effect. This behavior explains the difference found in the amplitude between experiment and theory at high wind speed despite the implementation of the Beddoes-Leishman dynamic stall model in the calculation.

Abbreviations

α: angle of attack [deg]; β: global pitch angle [deg]; φ_r: azimuth angle [deg]; φ_y: yaw angle [deg]; ρ: air density [kg/m^3]; Ω: rotor speed [rpm]; Γ: circulation [m^2/s]; A_0: angle of attack at which $CL_1 = 0$; for all AR (deg); ACL_1: angle of attack at maximum pre-stall lift (deg); ACD_1: angle of attack at maximum pre-stall drag (deg); B: blade number; BEM: blade element momentum theory; C: chord [m]; Cd: drag coefficient [dimensionless]; CD_0: minimum drag coefficient, at $\alpha = A_0$, for all aspect ratios; CD_1: drag coefficient in the pre-stall regime [dimensionless]; CD_2: drag coefficient in the post-stall regime [dimensionless]; CD_{1max}: maximum pre-stall drag coefficient; at α = ACD1 [dimensionless]; CD_{2max}: maximum post-stall drag coefficient [dimensionless]; Cl: lift coefficient [dimensionnelss]; CL_1: lift coefficient in the pre-stall regime [dimensionless]; CL_{1max}: maximum pre-stall lift coefficient; at $\alpha = ACL_1$ [dimensionless]; CL_2: lift coefficient in the post-stall regime [dimensionless]; DS: dynamic stall; r: radial position on the blade [m]; R: rotor radius [m]; $S1$: slope of linear segment of pre-stall lift curve (1/deg); U: wind velocity [m/s]; V_{ind}: induced velocity [m/s]; V_{rel}: relative wind speed velocity [m/s].

Competing interest

The authors declared that they have no competing interests.

Authors' contributions

AB, AA, and NB have participated in the development and validation of the calculation code. All authors have read and approved the final manuscripts.

Authors' information

All authors are currently university professors at ENSAM Meknes. AB is assigned to the Department of Mechanical Engineering. His research is in the field of renewable energy, mainly wind energy. AA and NB work and conduct their research at the energy Department in the energetic field and fluid mechanics.

Acknowledgments

The authors are grateful to the Director of ENSAM Meknes and the Director of doctoral studies center.

Author details

[1]Department of Mechanical Engineering, Moulay Ismail University, ENSAM-MEKENS, PO. BOX. 4024, Meknes 50003, Morocco. [2]Department of Energetic, Moulay Ismail University, ENSAM-MEKENS, P.O. BOX. 4024, Meknes 50003, Morocco.

Received: 10 May 2013 Accepted: 22 August 2013
Published: 09 Sep 2013

References

1. Lanzafame, R, Messina, M: Fluid dynamics wind turbine design: critical analysis, optimization and application of BEM theory. Renew Energ. **32**, 2291–2305 (2007)
2. Afjeh, AA, Keith Jr, TG: A vortex lifting line method for the analysis of horizontal axis wind turbines. Trans. ASME J. Sol. Energy Eng. **108**, 303–9 (1986)
3. Chkir, S: Unsteady loads evaluation for a wind turbine rotor using free wake method. Energy Procedia. **6**, 777–785 (2011)
4. Beddoes, TS: A near wake dynamic model. In: Aerodynamic and Acoustics National Specialist Meeting, pp. 1–9., Arlington, TX (1987)
5. Wang, T, Coton, FN: A modified near wake dynamic model for rotor analysis. Aeronaut J. **103**, 143–146 (1999)
6. Vermeer, LJ, Sorensen, JN, Crespo, A: Wind turbine wake aerodynamics. Prog Aerosp Sci **39**, 467–510 (2003)
7. Sebastien, T, Lackner, MA: Development of a free vortex wake method code for offshore floating wind turbines. Renew Energ. **46**, 269–275 (2012)
8. Hansen, MOL, Sørensen, JN, Voutsinas, S, Sørensen, N, Madsen, HA: State of the art in wind turbine aerodynamics and aeroelasticity. Prog Aerosp Sci. **42**, 285–330 (2006)
9. Leishman, JG: Principles of Helicopter Aerodynamics. Cambridge Universiy Press, Cambridge (2006)
10. Bhagwat, J, Leishman, J: Free-vortex filament methods for the analysis of helicopter rotor wakes. J Aircraft. **39**, 759–775 (2002)
11. Spera, DA: Models of lift and drag coefficients of stalled and installed airfoils in wind turbines and wind tunnels. Report NASA/CR—2008-215434. NASA, Cleveland, OH (2012)
12. Larsen, JW, Nielsen, SRK, Krenk, S: Dynamic stall model for wind turbine airfoils. J Fluid Struct. **23**, 959–982 (2007)
13. Leishman, JG, Beddoes, TS: A semi–empirical model for dynamic stall. J. Am Helicopter Soc. **34**(3), 3–17 (1989)
14. Galvanetto, U, Peiro, J, Chantharasenawong, C: Remarks on the nonlinear dynamics of a typical aerofoil section in dynamic stall. Aeronaut J. **111**, 731–739 (2007)
15. Dai, JC, Hu, YP, Liu, DS, Long, X: Aerodynamic loads calculation and analysis for large scale wind turbine based on combining BEM modified theory with dynamic stall model. Renew Energ. **36**, 1095–1104 (2011)
16. Huyer, H: Effects of forced unsteady separated flow fields on a rotating wind turbine blade. NREL Tech. Rep. 442–4864. Natl. Renewable Energy Lab, Golden, CO (1993)
17. Simms, D, Schreck, S, Hand, M, Fingersh, LJ: NREL unsteady aerodynamics experiment in the NASA-Ames wind tunnel: a comparison of predictions to measurements. National Renewable Energy Laboratory/TP-500-29494. Natl. Renewable Energy Lab, Golden, CO (2001)
18. Shepers, JG: IEA annex XX: comparison between calculations and measurements on a wind turbine in yaw in the NASA-Ames wind tunnel. ECN-E-07-072. Energy Research Center of the Netherlands, Petten (2005)
19. Leishman, JG: Challenges in modeling the unsteady aerodynamics of wind turbine. In: 21st ASME Wind Energy Symposium and 40th AIAA Aerospace Sciences Meeting., Reno, NV (2002)

10.1186/2251-6832-4-35
Cite this article as: Bouatem *et al.*: Load evaluation of horizontal-axis wind turbine rotor using coupled Beddoes near-wake model and free-wake method. *International Journal of Energy and Environmental Engineering* 2013, 4:35